



RESEARCH ARTICLE

10.1002/2016ea000240

Key Points:

- We model the radiation environment during the MSL cruise phase and on the Martian surface
- We obtain the particle energy spectra at the RAD instrument for both scenarios
- After developing a method to distinguish between upward and downward fluxes, we apply the method both to simulation data and to data taken by the RAD instrument during the cruise phase and on the surface

Correspondence to:

J. K. Appel,
appel@physik.uni-kiel.de

Citation:

Appel, J. K., Köehler, J., Guo, J., Ehresmann, B., Zeitlin, C., Matthä, D., ... Weigle, G. (2018). Detecting upward directed charged particle fluxes in the Mars Science Laboratory Radiation Assessment Detector. *Earth and Space Science*, 5, 2–18. <https://doi.org/10.1002/2016ea000240>

Received 23 NOV 2016

Accepted 20 OCT 2017

Accepted article online 15 NOV 2017

Published online 23 JAN 2018

Detecting Upward Directed Charged Particle Fluxes in the Mars Science Laboratory Radiation Assessment Detector

J. K. Appel¹, J. Köehler^{1,2}, J. Guo¹, B. Ehresmann³, C. Zeitlin⁴, D. Matthä⁵, H. Lohf¹, R. F. Wimmer-Schweingruber¹, D. Hassler³, D. E. Brinza⁶, E. Böhm¹, S. Böttcher¹, C. Martin¹, S. Burmeister¹, G. Reitz⁵, S. Rafkin³, A. Posner⁷, J. Peterson³, and G. Weigle⁸
¹Institute for Experimental and Applied Physics, University of Kiel, Germany, ²Thales Electronic Systems GmbH, Kiel, Germany, ³Southwest Research Institute, Boulder, CO, USA, ⁴Lockheed Martin Information Systems & Global Solutions, Houston, TX, USA, ⁵Aerospace Medicine, Deutsches Zentrum für Luft- und Raumfahrt, Köln, Germany, ⁶Jet Propulsion Laboratory, California Institute of Technology, Pasadena, CA, USA, ⁷Science Mission Directorate, NASA Headquarters, Washington, DC, USA, ⁸Big Head Endian, LLC, Burden, KS, USA

Abstract The Mars Science Laboratory rover Curiosity, operating on the surface of Mars, is exposed to radiation fluxes from above and below. Galactic Cosmic Rays travel through the Martian atmosphere, producing a modified spectrum consisting of both primary and secondary particles at ground level. These particles produce an upward directed secondary particle spectrum as they interact with the Martian soil. Here we develop a method to distinguish the upward and downward directed particle fluxes in the Radiation Assessment Detector (RAD) instrument, verify it using data taken during the cruise to Mars, and apply it to data taken on the Martian surface. We use a combination of Geant4 and Planetocosmics modeling to find discrimination criteria for the flux directions. After developing models of the cruise phase and surface shielding conditions, we compare model-predicted values for the ratio of upward to downward flux with those found in RAD observation data. Given the quality of available information on Mars Science Laboratory spacecraft and rover composition, we find generally reasonable agreement between our models and RAD observation data. This demonstrates the feasibility of the method developed and tested here. We additionally note that the method can also be used to extend the measurement range and capabilities of the RAD instrument to higher energies.

Plain Language Summary The MSL rover Curiosity is exposed to energetic particles from above and below on the Martian surface. Particles enter the Martian atmosphere from above and travel through it until they reach the ground. Particles lose energy and can produce secondary particles while passing through the atmosphere, resulting in an energy distribution on ground level that is different from that on the top of the atmosphere. The resulting particles produce an upward directed particle distribution in the soil. We develop a method to distinguish the upward and downward particle fluxes in the RAD instrument, verify it using data taken during the cruise to Mars, and apply it to data taken on the Martian surface. We use a combination of models to find criteria for discriminating the flux directions. After developing models of the cruise phase and surface shielding conditions, we compare simulated values for the ratio of upward to downward flux with those found in observation data. We find generally reasonable agreement between our models and RAD observation data. This demonstrates the feasibility of the method developed and tested here. The method can also be used to extend the measurement range and capabilities of the RAD instrument to higher energies.

1. Introduction

The Mars Science Laboratory (MSL) mission is an ongoing NASA mission. It successfully landed the rover “Curiosity” inside the Gale Crater on the surface of Mars on 6 August 2012 (Grotzinger et al., 2012). One of the scientific instruments on board the rover is the Radiation Assessment Detector (RAD), which measures the Martian radiation environment. It is able to measure charged particles $\geq 100 \frac{\text{MeV}}{\text{nuc}}$ (Hassler et al., 2012). RAD is designed to measure radiation entering the detector from above. The main science goals of the RAD instrument

©2017. The Authors.

This is an open access article under the terms of the Creative Commons Attribution-NonCommercial-NoDerivs License, which permits use and distribution in any medium, provided the original work is properly cited, the use is non-commercial and no modifications or adaptations are made.

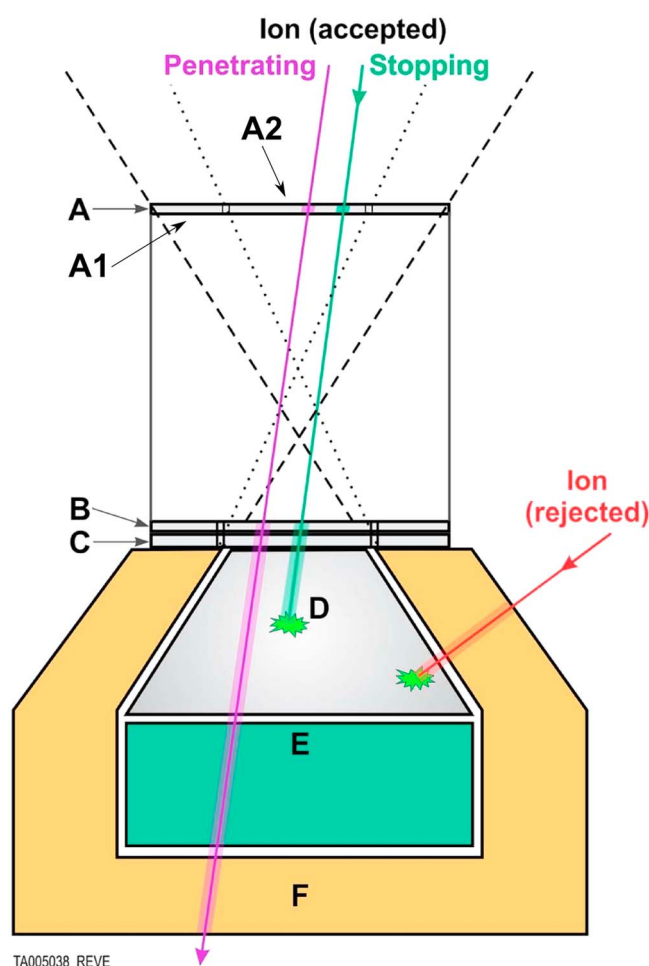


Figure 1. Schematic view of the RAD detector with various particle detections shown. The viewcone as defined by the A1-B coincidence (dashed) and by the A2-B coincidence (dotted) is shown, as are the names of the detectors. For the SSD, the segmentation borders are visible. (Ehresmann et al., 2014; modified from Hassler et al., 2012).

include characterizing the Martian radiation environment to enable validating models of atmospheric particle transport.

In this paper, we will present a method to discriminate between upward and downward directed charged particle fluxes above the particle energy range RAD is designed to measure. The application of this method significantly increases the instruments' capabilities for charged particle detection. In addition, it aids in validating the particle transport models used in this analysis.

RAD operated during most of the cruise phase from Earth to Mars, taking almost 220 days of data (Zeitlin et al., 2013). It has been operating on the surface of Mars almost continuously since the landing of the MSL rover on 6 August 2012 (Hassler et al., 2014). This provides us with a still growing data set spanning over 1,300 Martian days (sols) to date, including the full Martian annual cycle, which is about 668 sols, with 1 sol being about 1.03 Earth days long (Allison, 1997).

This paper is organized in the following way: After a short description of relevant features of the RAD instrument, we develop a method for discriminating upward and downward fluxes through simulations. The simulation results help us to test and pin down certain criteria of the method when applied to data. With these criteria, we apply the method to data of the radiation environment RAD measures both during the cruise phase and on the surface of Mars. We compare the findings from the modeling with data obtained both during cruise phase and on the Martian surface. Lastly, we assess the findings and discuss the accuracy of the models and transport codes used in this analysis.

1.1. The RAD Instrument

The Radiation Assessment Detector (RAD) is a compact and light-weight instrument designed to fully characterize the radiation environment on the Martian surface.

RAD derives heritage from the Comprehensive SupraThermal and Energetic Particle analyzer (COSTEP) instrument on SOHO (Müller-Mellin et al., 1995), the Matroshka instrument currently flying on the ISS (Reitz et al., 2009), as well as Böhm (2004) and Posner et al. (2005). A detailed description of RAD is given in Hassler et al. (2012). We describe briefly the features relevant to this investigation in the following paragraphs.

A schematic view of the RAD instrument is shown in Figure 1. It employs a detector stack consisting of three hexagonal silicon Solid State Detectors (SSD)

called detectors A, B, and C on top of two scintillation detectors, called D and E. Detector A is split into two segments, an outer segment called A1 and an inner segment called A2. The detectors B and C only use the inner segment of the detector. The scintillation detectors are enclosed in an anticoincidence shield made of another scintillation detector, F.

The D detector is a truncated hexagonal pyramid of thallium-doped Cesium Iodide (CsI(Tl)). The E scintillator is made of Bicron BC-432 m plastic scintillator and has an extruded hexagonal shape. BC-432 m is also used for the anticoincidence, F, which is split into two scintillators, F2 below the detector stack and F1 enclosing D and E from the side.

The two segments of the A detector, together with the inner segment of the B detector, define the two possible view cones of the RAD instrument. The A1-B coincidence viewcone uses the outer A1 segment, and the A2-B coincidence viewcone uses the inner A2-B viewcone, which is also fully covered by the D detector below it. As we will later show, our analysis requires particles to deposit energy in both the D and the E detector. Since only the A2-B viewcone is fully covered by the D detector, we only consider particles inside the A2-B viewcone in this work.

RAD is designed to measure protons and alpha particles entering the detector stack from above in an energy range between 10 MeV and 100 $\frac{\text{MeV}}{\text{nuc}}$.

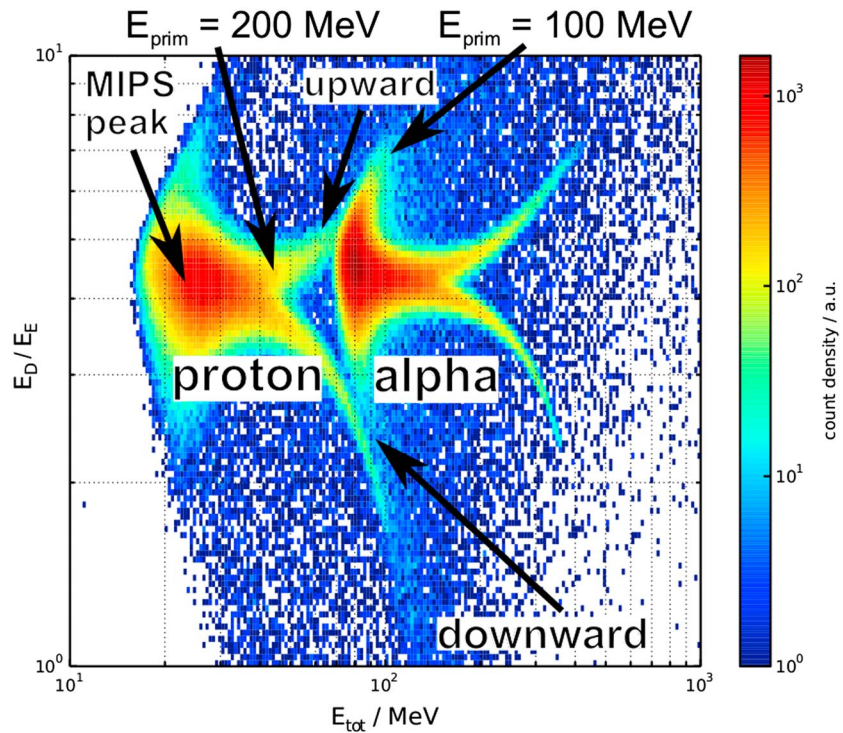


Figure 2. Two-dimensional count density histogram for simulation data of $\frac{E_D}{E_E}$ versus E_{tot} . The annotations denote particle species and beam directions.

2. Simulation Setup

We performed two major simulation steps in order to analyze the instrument response to upward directed particle fluxes. First, we develop criteria to distinguish between the upward and downward fluxes in RAD data. In order to do this, we simulated the passage of particles with a uniform energy spectrum through only the RAD instrument. After we found working discrimination criteria, we replicated the RAD measurement both inside the spacecraft during the cruise phase and on the Martian surface. This was achieved by first simulating the passage of particles through the surrounding geometry, which during the cruise phase consists of the MSL cruise stage and the rover itself, and on the surface consists of the Martian atmosphere and soil as well as the rover body. These models yielded the upward and downward directed spectra at the position of the RAD instrument. We then simulated the response of the instrument to these spectra and applied the discrimination method as developed in the first step of this analysis.

2.1. Upward and Downward Fluxes in the RAD Instrument

We simulated the passage of upward and downward directed particle fluxes through the instrument in two separate simulations using the GEANT4 toolkit (Agostinelli et al., 2003). We used version 10 of the toolkit, using the QGSP_BERT physics list, for all instrument and shielding simulations. The particle source for these simulations was a circular area positioned just above the A detector for downward and just below the F detector for upward directed radiation. The particles were emitted in beams parallel to the central axis of the RAD instrument with no angular distribution of the tracks. For the energy spectrum of the particles, a logarithmically flat spectrum from 100 MeV to 1 GeV was generated.

Based on the results of this simulation, we are able to discriminate the flux direction in the energy range between a primary particle energy of $E_{prim} = 100$ MeV and $E_{prim} = 200$ MeV by plotting the ratio between energy deposited in detectors D and E, namely, $\frac{E_D}{E_E}$, versus the total deposited energy $E_{tot} = E_{A2} + E_B + E_C + E_D + E_E$. Because we use energy deposited in detectors D and E for determining the flux direction, we need complete coverage of the telescope viewcone by those detectors. This is true for the narrower A2-B viewcone, so we only select particles within this viewcone.

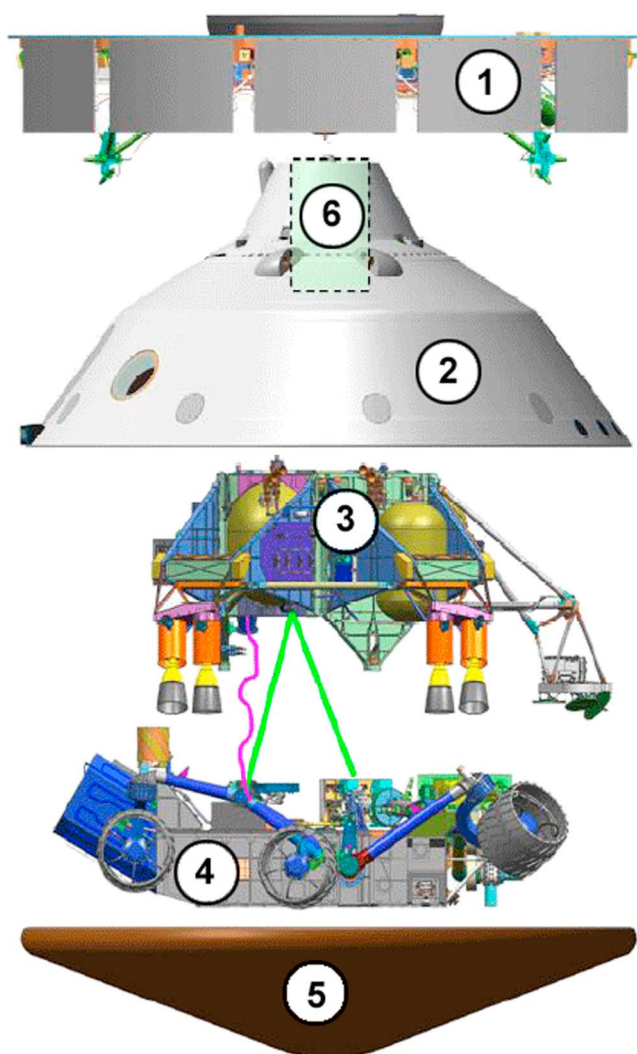


Figure 3. Schematic view of the components of the MSL cruise stage. The labeled parts are 1—cruise stage, 2—aeroshell, 3—descent stage, 4—MSL rover, 5—heatshield, and 6—parachute assembly (Image credit: NASA/JPL-Caltech).

The F detector is used as an anticoincidence shield for the telescope: particles that enter the instrument from below and deposit energy in the F detector get rejected by the detection logic. The exception to this is penetrating particles which deposit energy in all detectors of the stack. It is thus necessary to require penetrating particles in order to detect upward directed fluxes in the instrument.

We then plot $\frac{E_D}{E_F}$ versus E_{tot} in a 2-D count density histogram as shown in Figure 2. The distinctive proton and alpha particle populations are clearly visible. For each particle type, we find the peak intensity produced by the Minimum Ionizing ParticleS (MIPS) on the side of the population with the least deposited energy E_{tot} as expected from the Bethe-Bloch formula. As particles with smaller primary energies deposit more energy, we can discern the upward and downward branch.

For protons, the branches separate at a deposited energy of $E_{tot} \geq 42$ MeV up to an energy of $E_{tot} = 100$ MeV, where the particles do not penetrate the detector stack any longer. This corresponds to a primary proton energy range of $100 \text{ MeV} \leq E_{prim} \leq 200 \text{ MeV}$ for which we are able to separate the particle direction.

This discrimination can, in principle, be applied to all charged particles detected with the RAD instrument. However, we will only present the analysis for protons, because protons are the most common particles in these environments, particularly among the secondary particles coming from the surface (e.g., Ehresmann, 2014; Matthiä et al., 2016).

2.2. The RAD Shielding Environment During the MSL Cruise Phase

During the cruise phase, the instrument was not only shielded from upward directed particles by the rover, but the rover itself was shielded inside the MSL spacecraft, consisting of four main parts: The descent stage mounted above the rover, the aeroshell and heatshield surrounding both rover and descent stage, and the cruise stage mounted above the aeroshell. A schematic of this configuration is shown in Figure 3. This leads to a highly inhomogeneous shielding in the upper viewcone of the RAD instrument, where particles are shielded by the descent stage, the aeroshell, and the cruise stage. While approximately half of the field of view is almost unshielded, the other half is shielded by various amounts of mass. The lower viewcone is shielded by the rover body itself and the heatshield.

For the simulation of upward and downward particle fluxes during the cruise phase, we employed a separate simulation for each direction. Both simulations use a square source area with a side length of $l = 10 \text{ cm}$ from which the primary particle spectra were generated as parallel beams. The particle beams then passed through the shielding masses before being registered in a vacuum volume used for particle counting.

Upward directed particles are shielded both by the rover body and by the aeroshell, which in this part is the heat shield for the atmosphere entry. The rover body is represented by two blocks of different materials: the rover bellypan consisting of a 5 mm aluminum plate, followed by the rover body filled with electronics with a height of 29 cm. The best data available to the authors states that the rover body is dominated by the RAD Electronics Box (REB) with a shielding density of 6 g cm^{-2} , consisting of Printed Circuit Boards (PCBs) plus magnesium to account for the REB housing. The chemical composition of PCBs is taken from Ogunniyi et al. (2009). The heatshield is positioned directly below the rover bellypan. It is represented by a 3.2 cm high block of carbon with a density of $0.27 \frac{\text{g}}{\text{cm}^3}$ (Tran et al., 1996; Edquist et al., 2014). The composition, densities, and dimensions of the different blocks are given in Table 1.

The shielding density distribution for the upper viewcone is described in Zeitlin et al. (2013) as shown in Figure 4. From this we approximate the shielding as 10 blocks of aluminum with varying thickness according to the integrated shielding density inside the instrument viewcone. A histogram of this distribution inside

Table 1
Composition and Density of Simulation Boxes

| Block | Density | Composition |
|-------------|--------------------------------------|------------------------|
| Heatshield | $0.27 \frac{\text{mg}}{\text{cm}^3}$ | C: 100% |
| Belly plate | $2.7 \frac{\text{g}}{\text{cm}^3}$ | Al: 100% |
| | | Cu: 20% |
| | | SiO ₂ : 15% |
| | | PET: 9.9% |
| | | PP: 4.8% |
| Rover body | $0.183 \frac{\text{g}}{\text{cm}^3}$ | Al: 2% |
| | | Pb: 2% |
| | | Ni: 2% |
| | | Fe: 8% |
| | | Sn: 4% |
| | | Mg: 30% |

Note. the percentage values of the electronics material are normalized to 100%.

the A2-B coincidence angle is shown in Figure 5. In reality, not all material is aluminum, for example, the propellant tanks contain Hydrazine. However, since the distribution available to us is stated as being aluminum equivalent, we use pure aluminum for the shielding blocks.

For both the upward and downward particle spectra simulations, the primary particle spectra consisted of proton and alpha particle spectra generated by the Badwar-O'Neill Galactic Cosmic Ray (GCR) model (BO10) (O'Neill, 2010). We use a solar modulation parameter of $\Phi = 627.38$ MV as input for the model, which corresponds to the modulation during the MSL cruise phase (Usoskin et al., 2011). The spectra were computed for a distance of 1 AU. However, the radial gradient of the GCR is on the order of 3% per AU (Gieseler & Heber, 2016). The error induced by the different GCR spectra at Mars' orbit, with a radius of approximately 1.5 AU, is therefore very small when compared to other uncertainties. In addition, the change will tend to balance out in comparison to the underestimation the BO10 will make of the GCR flux when compared to more recent models.

It should be noted that we use parallel particle beams for the cruise phase shielding simulations. In contrast to that, the shielding simulations for the Martian surface, as described in the next section, use angular distributions for the particles generated. The final shielding geometry used in the simulation is also extremely simplified from the real geometry seen in Figure 3. The rationale behind this is that given the uncertainties and the large number of unknowns in the description of the geometry, and given the fact that the GCR has an isotropic angular distribution, our simplified model will be sufficient to reproduce the shielding situation as it is known to the authors.

2.3. The RAD Shielding Environment on the Martian Surface

Next, we attempt to simulate the 2-D count density histogram as expected from data taken by RAD on the Martian surface. This is done using an approach consisting of three different modeling steps: First, we use the Planetocosmics code (Desorgher et al., 2006) to determine the expected spectra and intensities of upward and downward directed particles on the Martian surface. Second, the upward directed part of the spectrum

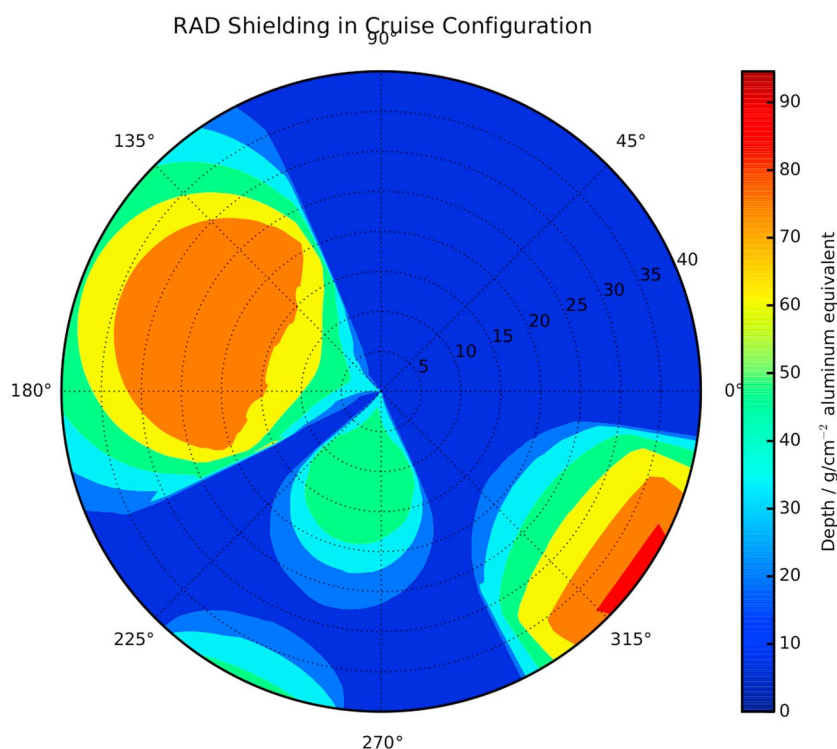


Figure 4. Distribution of shielding densities in the upper A1-B coincidence angle viewcone of the RAD instrument during cruise phase. Note that this shows the full viewcone, while the analysis in this paper only considers the inner viewcone ($0^\circ \leq \theta \leq 18^\circ$). Taken from Zeitlin et al. (2013)

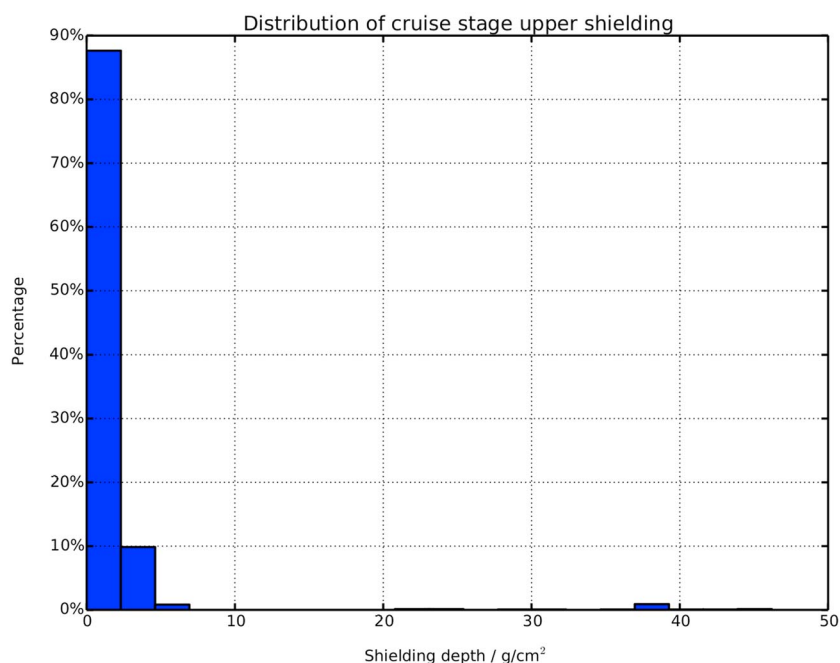


Figure 5. Histogram of shielding distribution inside the upper RAD instrument viewcone as used for constructing the simulation shielding model. It is evident that almost the entire upper viewcone is unshielded.

passes through the body of the MSL rover before being measured by the RAD instrument. This is simulated by modulating the upward Planetocosmics generated spectrum by a second GEANT4 simulation representing the MSL rover body. Finally, we simulate the instrument response to the downward spectra obtained from the Planetocosmics simulations and the upward spectra obtained from the rover body simulation. We then use the results from the RAD instrument simulation to build the 2-D count density matrix as described in section 2.1 and similar to that shown in Figure 2.

We used a version of Planetocosmics updated to utilize Geant4 version 9.6, configured to use the PHITS code (Niita et al., 2006) for ion hadronic interactions, the QGSP_BIC_HP physics list for hadronic interactions, and the emstandard_opt4 physics list for electromagnetic interactions. The simulations for determining the upward and downward directed spectra on the Martian soil were done using a planar geometry with a side length of $l = 3,000$ km to avoid particle losses at the simulation boundaries. We used the Mars Climate Database (Forget et al., 2006) as a model atmosphere, with the atmospheric height being $h = 250$ km. The atmosphere profile is extracted at the location of Gale Crater, using the climatology model, which corresponds to a normal amount of atmospheric dust loading (Forget et al., 2006). The surface pressure of the model atmosphere is $p = 842.72$ Pa, which is the mean pressure during the observation interval (Haberle et al., 2014). The Martian regolith is represented in the Planetocosmics simulation by a 100 m thick layer of SiO_2 with a mass density of 1.7 g cm^{-2} . While this does not represent the exact composition of the soil, we have found through preliminary simulations that this simplification of soil composition does not significantly influence the upward directed particle spectra in the energy range interesting to us. The depth of the soil layer chosen is sufficient to accommodate the maximum of secondary particle production, which occurs at a depth of approximately 1 m (Morthekai et al., 2007).

The input spectra at the top of the Martian atmosphere were proton and alpha particle spectra taken from the Badwar-O'Neill GCR model as used in section 2.2.

The simulation geometry for simulating the MSL rover body uses a cube with a width and depth of $l = 10$ m and a height of $h = 1$ m. The cube consists of four blocks of different materials: From the bottom, there is a 60 cm high block representing the Martian atmosphere, followed by a 5 mm aluminum plate representing the rover bellypan. This is followed by the MSL rover body as described in section 2.2 with a height of 29 cm, and lastly by a 10.5 cm high block of vacuum used as a particle counting volume. The composition, densities, and dimensions of the different blocks are given in Table 2.

Table 2
Composition, Density and Height of Simulation Boxes

| Block | Density | Height | Composition |
|-------------|--|---------|--|
| Atmosphere | $1.92 \cdot 10^{-5} \frac{\text{mg}}{\text{cm}^3}$ | 29.0 cm | CO ₂ : 95.7% N: 2.7% Ar: 1.6% |
| Belly plate | $2.7 \frac{\text{g}}{\text{cm}^3}$ | 0.5 cm | Al: 100% Cu: 20% SiO ₂ : 15% PET: 9.9% PP: 4.8% |
| Rover body | $0.183 \frac{\text{g}}{\text{cm}^3}$ | 29.0 cm | Al: 2% Pb: 2% Ni: 2% Fe: 8% Sn: 4% Mg: 30% |

Note. The percentage values of the electronics material are normalized to 100%.

The particle source used in the simulations is configured to emit particles in an angular distribution predicted by the Planetocosmics simulations from the bottom area of the simulation. The source uses the upward directed proton, alpha, and neutron particle spectra resulting from the Planetocosmics simulations as described above for generating energy spectra.

Upward directed particle spectra for the RAD instrument simulation are generated from proton and alpha particles reaching the topmost vacuum layer of the simulation. We select only the particles that are within the inner RAD A2-B viewcone of 18°. The downward directed particle spectra are taken directly from the Planetocosmics simulation. We use the downward directed proton and alpha particle spectra from particles selected to be within the inner RAD viewcone.

3. Simulated Particle Fluxes in the RAD Instrument

In the following sections, we describe the particle spectra resulting from our simulations. For the cruise phase, these are the spectra calculated by the shielding simulation inside the MSL spacecraft. The spectra on the Martian surface are from Planetocosmics and the rover body shielding simulation. We describe the particle spectra in an energy range from 10 MeV to 10 GeV, spanning the energy range used in our simulations.

3.1. Cruise Phase Particle Fluxes

The particle spectra derived for the cruise phase are shown in Figure 6.

It is immediately evident that the spectral shape of proton and alpha particle fluxes are largely unchanged, both for the upward and for the downward directed fluxes. Both particle types are also shielded more strongly in the downward direction than in the upward direction.

When comparing integrated particle fluxes in the range from 10 MeV to 10 GeV, the proton upward directed fluxes at RAD are reduced to 92.7% of GCR flux. Downward directed proton fluxes are reduced to 83.7% of GCR flux. In the same energy range, upward directed alpha particle fluxes are reduced to 82.6% of GCR flux, while downward directed alpha particle fluxes are reduced to 69.1% of GCR flux.

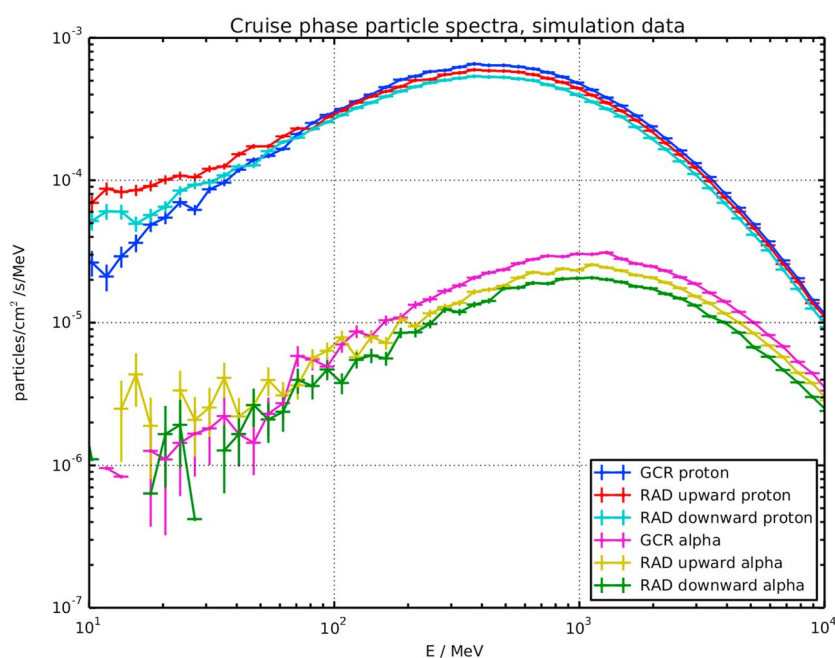


Figure 6. Comparison of downward and upward directed charged particle spectra during the cruise phase outside the spacecraft (labeled as primary) and at the RAD instrument. The fluctuations of the alpha particle spectra below 70 MeV are due to numerical effects.

Table 3
Ratios for Integrated Particle Fluxes During Cruise Phase for Different Particle Species

| Particle | $\frac{\text{RAD up}}{\text{GCR}}$ | $\frac{\text{RAD down}}{\text{GCR}}$ |
|----------|------------------------------------|--------------------------------------|
| Proton | 0.927 | 0.837 |
| Alpha | 0.826 | 0.691 |

Note. The ratios are computed for energies between 10 MeV and 10 GeV.

In total, integrated alpha particle fluxes are shielded more strongly than protons, with the difference between the two particle species being 10.1% for upward and 14.6% for downward directed fluxes. Both particle species experience no large reductions in flux due to the spacecraft shielding when compared to the GCR fluxes outside the spacecraft. We summarize the ratios of GCR flux to particle fluxes at the position of RAD in Table 3 for individual particles.

3.2. Particle Fluxes on the Martian Surface

Next, we describe the particle fluxes predicted by our simulations on the Martian surface. Here we have particle fluxes at several different places: On top of the atmosphere, we have the GCR flux, as before for the cruise phase. On the Martian surface, we have the upward and downward particle fluxes as predicted by the Planetocosmics simulation, as well as the upward directed particle fluxes at RAD. The latter, as described in section 2.1, is the upward directed fluxes inside the rover body at RAD, taken from the rover body simulation using the Planetocosmics upward directed fluxes as input.

We show the downward particle fluxes on the Martian surface in Figure 7. While the alpha particle fluxes show the same spectral shape, the proton fluxes are shifted toward a maximum at lower energies. We integrate particle fluxes between 10 MeV and 10 GeV and find that the downward proton flux on the Martian surface is attenuated to 84.2% of GCR flux at the top of the atmosphere. For alpha particles, the flux is reduced to 79.4% of GCR flux.

The upward particle fluxes on the Martian surface are shown in Figure 8. We note that for alpha particles, there are only very low upward fluxes at low energies on the Martian surface, and no particle fluxes inside the rover body at RAD. Protons show a more pronounced upward directed flux, which gets shielded by the rover body below an energy of approximately 300 MeV.

The upward directed alpha particle flux on the Martian surface is 0.02% of the GCR flux, and the proton upward directed flux on the surface is 6.7% of GCR flux. Our simulations predict no upward alpha particle fluxes at RAD. The proton upward flux at RAD is reduced to 52.9% of the upward flux on the Martian surface. When compared to the downward flux on the surface, the upward flux at RAD is reduced to 4.2%. The ratios for the different fluxes are summarized in Table 4.

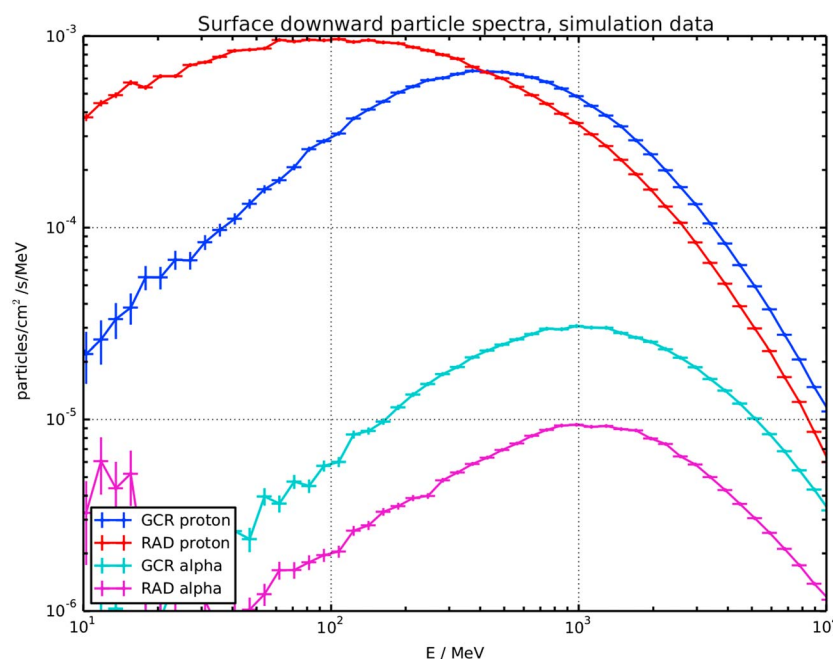


Figure 7. Comparison of GCR particle spectra to downward directed spectra on the Martian surface at soil level. Spectra labeled as primary are the downward GCR spectra on top of the atmosphere.

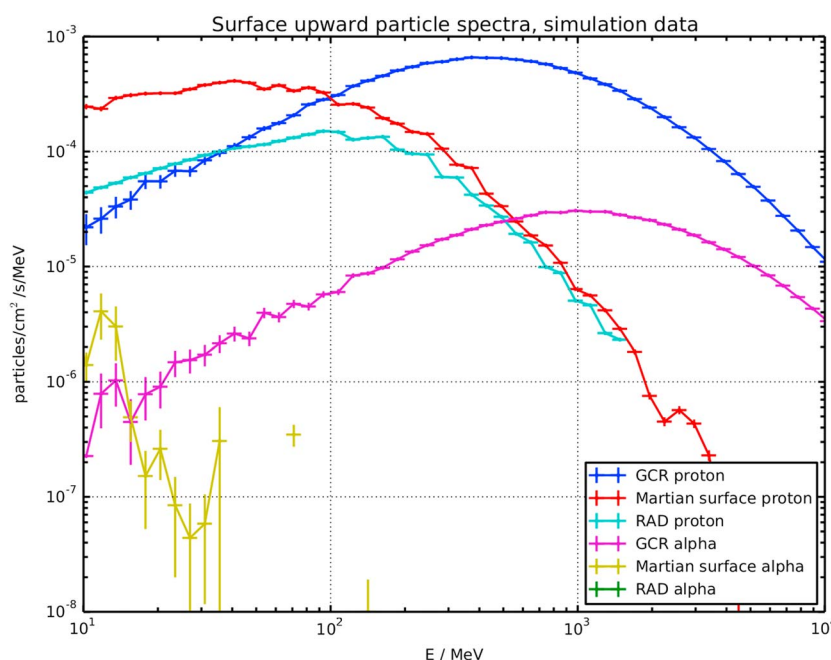


Figure 8. Comparison of GCR particle spectra to upward directed spectra on the surface at soil level and inside the rover body. Spectra labeled as primary are the downward GCR spectra on top of the atmosphere. There are no upward directed alpha particle fluxes predicted inside the rover body.

3.3. Determining Flux Ratios

To discriminate between upward and downward directed fluxes, the method we show in section 2.1 relies on energy deposits in both the D and E scintillator. It is similar to work done by Sierks (1997) for SOHO/Electron, Proton, Helium Instrument (EPHIN) and based on the method presented in McDonald and Ludwig (1964). The use of detector F as an anticoincidence shield means that particles entering the instrument from below will not get registered. The exception to this is penetrating particles that deposit energy in each detector of the instrument. Protons start penetrating RAD at about $E_{\text{prim}} = 100$ MeV, which therefore is the lower boundary for the primary particle energy range in which the flux directions can be distinguished. The upper boundary is given by the point where the two branches merge into the MIPS peak.

For protons, this happens at a primary particle energy of about $E_{\text{prim}} = 200$ MeV. We list the mean energy deposits for protons in the D and E detectors in Table 5. If we compare the $\frac{E_D}{E_E}$ values for the two primary energies shown, we can clearly see that while the values are vastly different for $E_{\text{prim}} = 100$ MeV, they are almost equal at $E_{\text{prim}} = 200$ MeV. We also list the total deposited energy E_{tot} in Table 5, giving us a range of approximately $45 \text{ MeV} \leq E_{\text{tot}} \leq 100 \text{ MeV}$ in which we are able to separate particle flux directions.

The flux intensities of the branches were not derived as absolute values. Instead, the ratio of upward to downward directed flux $R = \frac{I_{\text{up}}}{I_{\text{down}}}$ was computed. To precisely determine the intensity I of the flux directions, we needed to avoid contamination by alpha particles or background. We achieved this by using an integration

Table 4

Ratios of Integrated Fluxes for Different Particle Types on the Martian Surface for Particle Energies Between 10 MeV and 10 GeV

| Particle | Upward Downward | RAD Upward | RAD Downward | Downward GCR | Upward GCR |
|----------|--------------------|---------------|-----------------|-----------------|---------------|
| Proton | 0.079 | 0.529 | 0.042 | 0.842 | 0.067 |
| Alpha | 0.0005 | NA | NA | 0.794 | 0.0002 |

Note. Here downward means downward directed flux at soil level, upward means upward directed flux at soil level before passing the rover, and RAD means upward flux at the RAD instrument after passing the rover. GCR is downward directed GCR fluxes on top of the Martian atmosphere. NA, not application.

Table 5
Mean Energy Deposits in the D and E Detector for Upward and Downward Directed Protons at Different Primary Particle Energies

| | $E_{\text{prim}} = 100 \text{ MeV}$ | | $E_{\text{prim}} = 200 \text{ MeV}$ | |
|-----------------------------|-------------------------------------|----------------|-------------------------------------|-----------------|
| | Upward | Downward | Upward | Downward |
| E_D/MeV | 81.3 ± 16.5 | 57.9 ± 3.1 | 37.9 ± 10.1 | 36.3 ± 9.4 |
| E_E/MeV | 13.2 ± 2.3 | 24.3 ± 3.4 | 8.7 ± 2.2 | 9.5 ± 2.9 |
| $\frac{E_D}{E_E}$ | 6.2 ± 2.3 | 2.4 ± 0.5 | 4.4 ± 2.3 | 3.8 ± 2.1 |
| $E_{\text{tot}}/\text{MeV}$ | 96.7 ± 16.4 | 83.2 ± 5.9 | 47.4 ± 10.5 | 46.5 ± 10.3 |

Note. The uncertainties are given by the standard deviation of the selected particles.

method we call branch integration. In the following, we explain this process, using the simulation data shown in Figure 2 as an example.

When plotting the ratio $\frac{E_D}{E_E}$ for one value of total deposited energy E_{tot} , we see upward and downward particles in separate branches as shown earlier in Figure 2. We first select the line of each branch manually in order to obtain a curved path of the branch to follow in the later integration steps. This integration path follows the visual maximum of each branch. As an example, we show the selected upward integration path for simulated cruise phase data as the black line in Figure 9 (left).

Next, we use additional masking to remove the contamination by alpha particles. This contamination can most easily be seen in the upward branch around $E_{\text{tot}} \approx 100 \text{ MeV}$. We use a polygonal mask in the $\frac{E_D}{E_E}$ versus E_{tot} histograms to remove alpha particle contaminations from the proton data. An example for this mask is shown in Figure 10.

We then integrate the counts contained in the branches. This is done as a two-step process: First, we take single slices in the $\frac{E_D}{E_E}$ axis for each branch, following the selected integration line. We shift the $\frac{E_D}{E_E}$ position for each individual slice of a branch so that they are positioned at the same point. Then, we add all profiles for one branch to obtain the total $\frac{E_D}{E_E}$ profile for that branch. We use the method of shifting the individual profiles to avoid broadening the peak of the branches' profile, which would otherwise happen due to the varying

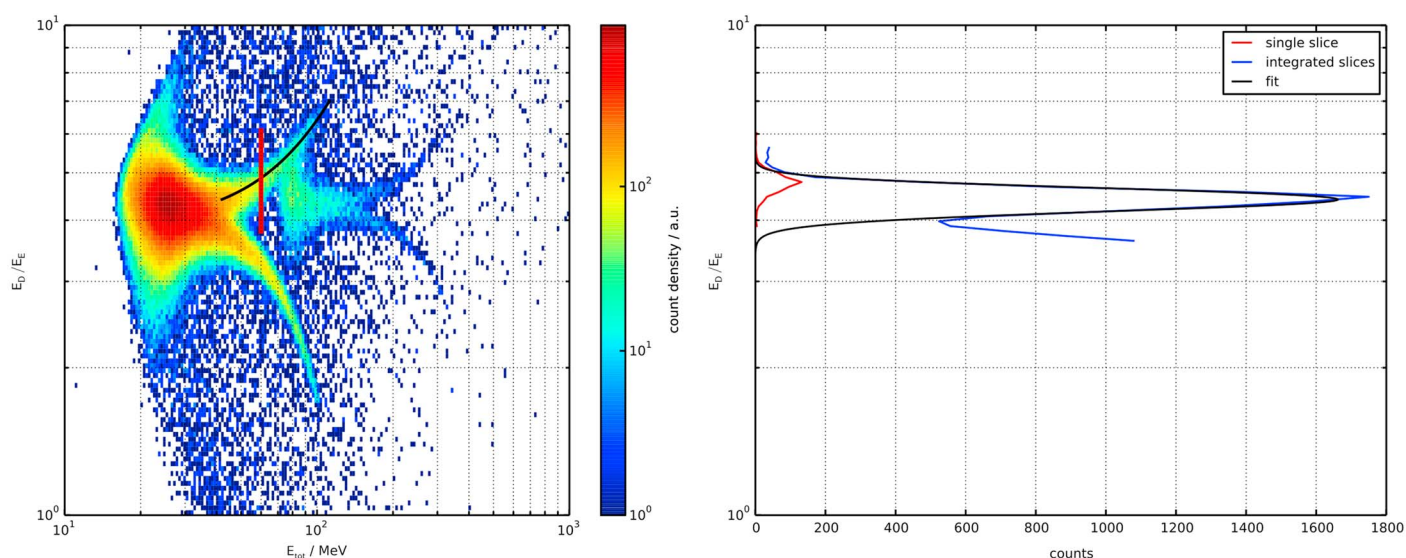


Figure 9. Example demonstrating the branch integration technique used in this analysis on the upward branch of simulated cruise phase data. (left) The data set used in the analysis. The black line is the manually selected integration line for the upward branch. The red line shows the position and extent of one of the slices taken for the branch integration process. (right) The integration results. The red line is the $\frac{E_D}{E_E}$ profile obtained from the single slice marked red in the left figure, which has not yet been shifted in its position on the $\frac{E_D}{E_E}$ axis. The blue line shows the result of the summation of the shifted $\frac{E_D}{E_E}$ profiles of all slices. Note the contamination with alpha particles visible in the profile for $\frac{E_D}{E_E} \leq 4$. The black line is the result of the Gaussian fit to the integrated slices, which is used to obtain the flux intensity of the branch.

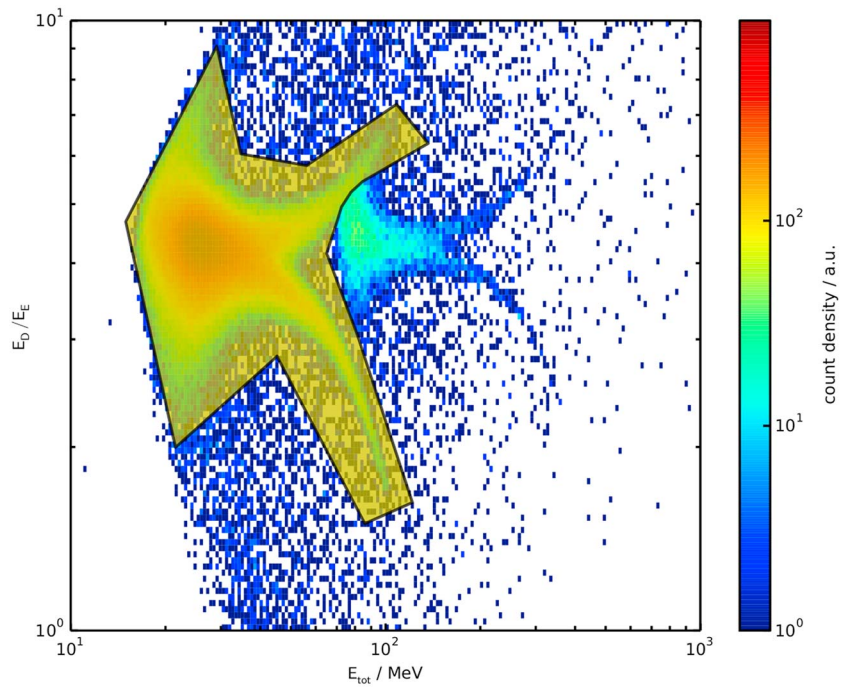


Figure 10. Mask used to separate protons from alpha particle contaminations. The polygonal mask is shown as yellow shade on top of a plot of simulated cruise phase data.

position on the $\frac{E_D}{E_E}$ axis. The position and extent of an individual slice used for integration is shown as a red line in Figure 9 (left) with the corresponding $\frac{E_D}{E_E}$ profile shown in Figure 9 (right). The sum of all individual slices is shown in Figure 9 (right) as a blue line.

In the second integration step, we fit the $\frac{E_D}{E_E}$ profile obtained with a Gaussian and integrate the area below it. This eliminates the background counts that may be present in the profiles. We show the result of the Gaussian fit to the integrated slices in Figure 9 (right) as a black line. Note that the fitted profile excludes the alpha particle contamination visible for $\frac{E_D}{E_E} \leq 4$. The area below the $\frac{E_D}{E_E}$ profiles for the upward and downward branches corresponds to the flux intensity I_{up} and I_{down} for each of the branches. We can then compute the ratio $R = \frac{I_{up}}{I_{down}}$.

In the case of simulation data using parallel beams with no spacecraft shielding as shown in Figure 11, this results in a ratio of $R = 0.77 \pm 0.06$.

In order to calculate the expected flux ratios from simulation data, one needs to be careful when combining the simulation runs for different particle species. We first performed the branch integration on the RAD instrument simulation for each individual particle species. The resulting areas are then scaled by the fluxes obtained from the rover body or the Planetocosmics simulations, respectively. Lastly, we compute the upward to downward flux ratio from the scaled areas.

3.4. Flux Ratios in Simulation Data

The 2-D histogram of the simulated fluxes during the cruise phase is shown in Figure 11. When computing the flux ratio R for an isotropic radiation field, a ratio of $R \approx 1$ can be expected. From the simulation data, the branch integration yields a flux ratio of $R = 0.98 \pm 0.08$.

The 2-D histogram for the simulated surface data set is shown in Figure 12. The integration of the branches yields a flux ratio of $R = 0.10 \pm 0.01$.

4. Observations of Upward Proton Flux

After having developed the method using simulation data and having applied it to simulated cruise phase and surface data, we now apply it to RAD measurements.

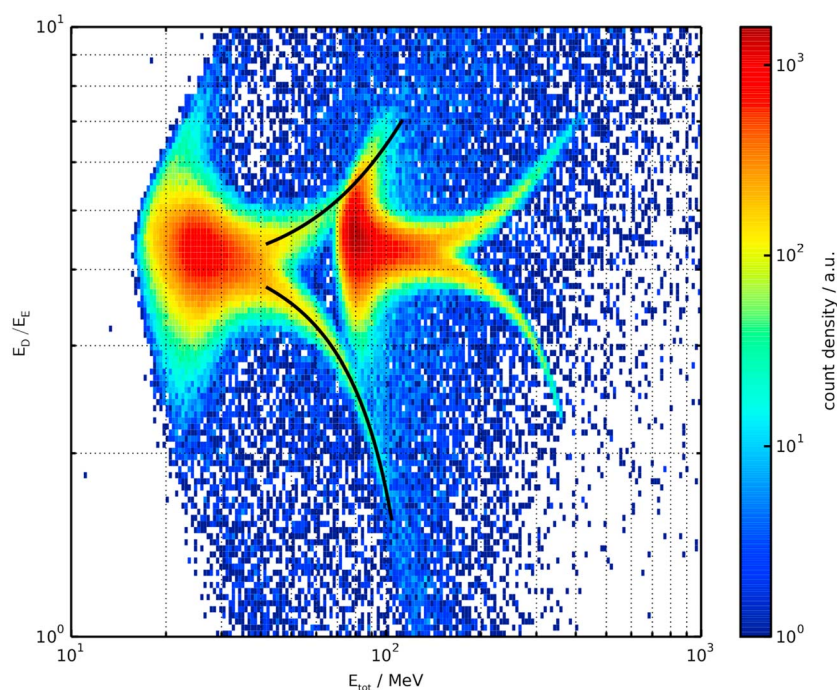


Figure 11. Selected integration lines for integrating along the upward and downward branches in simulation data for parallel particle beams entering the RAD instrument from above and below. The lines are shown in black above the proton upward and downward directed branches. Note that the simulation data shown in this plot is filtered to only contain penetrating particles.

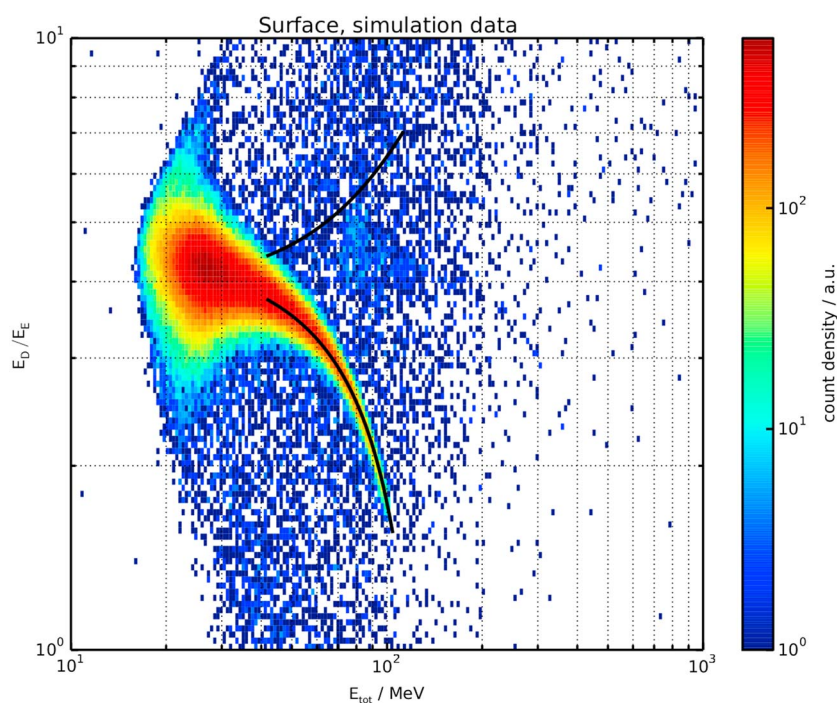


Figure 12. Selected integration lines for integrating along the upward and downward branches in simulation data for Martian surface radiation conditions. The lines are shown in black above the proton upward and downward directed branches. Note that the simulation data shown in this plot is filtered to only contain penetrating particles.

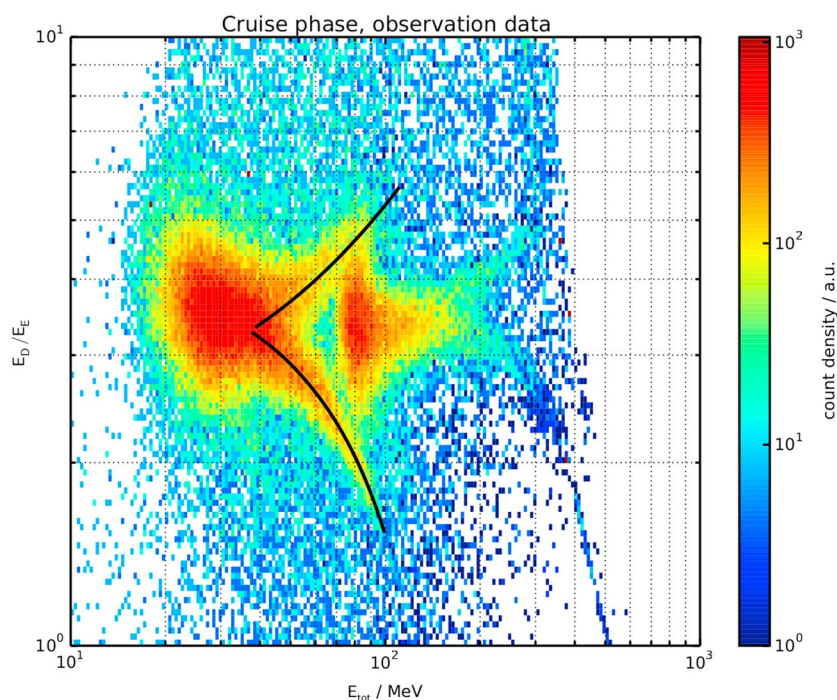


Figure 13. Selected integration lines for integrating along the upward and downward branches in cruise phase observation data. The lines are shown in black above the proton upward and downward directed branches. The difference in position on the $\frac{E_D}{E_E}$ axis when compared to simulation and surface data is due to instrument calibration.

4.1. Cruise Phase Data

We analyzed days 1 to 195 of the MSL cruise phase. We exclude all solar particle events, resulting in a total length of 163 days. The integration paths for integrating the branches are shown in Figure 13. The flux ratio derived from this is $R = 0.74 \pm 0.13$.

In RAD cruise phase data, the ratio of upward to downward flux in observation data agrees with the ratio predicted by the simulation using beams of equal intensities without the spacecraft shielding geometry. The ratio predicted by the simulation reproducing shielding conditions inside the MSL spacecraft predicts a 30% higher upward to downward flux.

However, we do not know the shielding conditions in detail, and the simulation uses a simplified geometry. As described in section 2.2, we reduce the geometry to a set of aluminum blocks, whereas the actual spacecraft is made of components of different materials in a complex arrangement. For a uniform shielding distribution, the modification of primary spectra by the shielding should not change the upward downward ratios.

For nonuniformly distributed shielding, upward and downward directed particle fluxes can be shielded differently. This leads to different spectra in the two directions, even when the primary spectra outside the shielding are identical, as would be the case for GCR. Finally, the nonuniform shielding distribution would, even for identical upward and downward fluxes, lead to a change in the upward to downward ratio.

In conclusion, the discrepancy of 30% between simulation results and the observations is a result of the uncertainties in using the simulation setup as described in section 2.2.

4.2. Surface Data

We analyzed surface data for 463 sols, starting from sol 1 to sol 500, again excluding all solar particle events. We note that even when selecting a long time range like the one used here, the upward directed flux is still very low. This is another reason we employed the branch integration process described in section 3.3, which allows us to separate the signal from unwanted contaminations as cleanly as possible. For the branches as shown in Figure 14, we derive a flux ratio of $R = 0.10 \pm 0.02$.

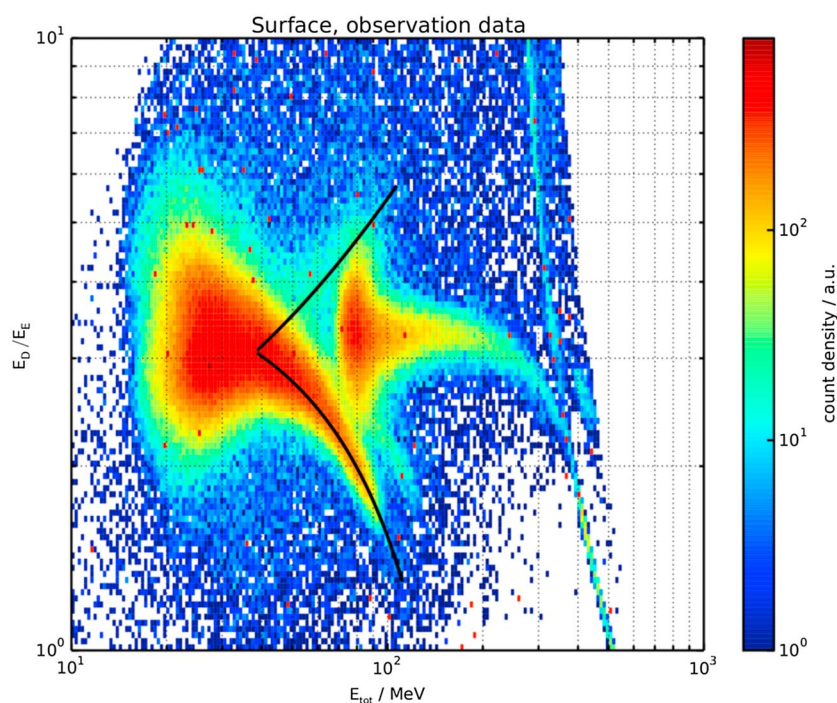


Figure 14. Selected integration lines for integrating along the upward and downward branches in surface observation data. The lines are shown in black above the proton upward and downward directed branches. The difference in position on the E_D/E_E axis when compared to simulation and cruise phase data is due to instrument calibration.

5. Discussion

The flux ratios for cruise phase and surface data as well as the corresponding simulation results are shown in Table 6.

The results already consider the numerical uncertainties in the method, which are due to the counting statistics in the simulation. There are other factors influencing the results, of which we list four here and discuss them below:

First, the rover body composition and thus the shielding for the upward directed radiation is not well known, as seen for the results obtained for the cruise phase. Second, the simulation considers only a perfectly even Martian surface with the rover body at all times being perfectly parallel to the surface. However, in reality, local topography will produce variations from these ideal conditions. Third, the influence of secondary particles generated inside the rover body has not been fully considered in this work. Finally, the upward and downward directed particle spectra modeled by the Planetocosmics simulation might not agree well with the real spectra seen on the Martian surface due to uncertainties of the primary spectra, the atmospheric, and soil properties as well as the choice of model and the physics processes considered in the model. We now discuss these four factors in some more details.

The influence of an only partially known shielding geometry has been described in the cruise phase results. We found a discrepancy of approximately 30% between measured and simulated upward to downward flux ratio. This discrepancy is most probably due to the unknowns in shielding geometry and composition. In the

simulations for the Martian surface, we only need to consider the lower part of the shielding, since the upper viewcone of the RAD instrument is unshielded by spacecraft structures and the composition and structure of the Martian atmosphere is well known. On the Martian surface, we find good agreement between simulation and observation data. Given that the shielding situation on the surface contains fewer unknowns than the shielding situation during the cruise phase, the good agreement we find is consistent with our conclusions for the cruise phase data. Additionally, we can conclude that the composition and

Table 6
Results of Upward to Downward Flux Ratio Calculations for Cruise Phase and Surface Simulations and Observation Data Sets

| | Cruise phase | Surface |
|-------------|-----------------|-----------------|
| Simulation | 0.98 ± 0.08 | 0.10 ± 0.01 |
| Observation | 0.74 ± 0.13 | 0.10 ± 0.02 |

structure of the rover body is known well enough to allow accurate simulation of the radiation environment on the Martian surface.

The simulation setup for Martian surface conditions assumes a perfectly flat surface with the rover being parallel to it. In reality, however, the surface can be uneven or tilted. Additionally, the terrain next to the rover can be higher or lower than beneath it. This can lead to shielding of the incoming GCR in the upper hemisphere, as well as allowing more of what is here considered the upward directed fluxes to arrive at the instrument. In total, this would lead to a higher upward to downward ratio. However, the observation data used in this analysis cover a long time span, and we only consider particles inside the narrow acceptance angle of about 18° in the vertical direction defined by the A2 and B detectors. The downward flux in this angular range has been shown to be close to isotropic, with only a small amount of shielding (Wimmer-Schweingruber et al., 2015). Based on this, we do not assume that local topography will have a major influence on this analysis. In the future, however, we hope to apply more sophisticated simulations including the tilting of the rover as well as realistic shielding by nearby mountains.

Secondary particles can be generated in the rover body both by upward and downward directed particle fluxes. The simulation setup we used for simulating particle fluxes on the Martian surface does not consider secondary particles generated in the rover body by downward fluxes. We only include secondary particles generated by upward fluxes from the Martian soil. However, the mass of the rover body is miniscule in comparison to the mass of the planet below it. Thus, downward directed particles will mainly produce upward directed secondary particle fluxes from the Martian soil.

The question of how well the particle spectra predicted by the Planetocosmics simulation agree with observed particle spectra is explored in Matthiä et al. (2016). The authors find good agreement between particle spectra measured by the RAD instrument and those predicted by the Planetocosmics simulation code for particle energies below 110 MeV. This suggests that the agreement between measured and simulated particle spectra will be sufficiently good for higher energy ranges as well. However, while Matthiä et al. (2016) considers the influence of high-Z particles in their work, we only consider proton and alpha particles as GCR primaries in our Planetocosmics simulations. Also, their work only treats the downward directed particle fluxes. The upward directed fluxes are not compared in Matthiä et al. (2016) and may be incorrectly predicted by Planetocosmics. Additionally, different solar modulations and atmospheric conditions may result in somewhat different results. Besides, the shielding of the primary fluxes through the atmosphere is also varying as the surface pressure changes seasonally (Guo et al., 2015).

Other authors (Gronoff et al., 2015) have compared the results of different transport models for the Martian surface, in particular the HZETRN code and Planetocosmics. While the upward fluxes are not reported by them, they find good agreement between both models. While it seems plausible that similar modeling results to those we present here could be obtained using other transport codes, the general agreement lets us conclude that our choice of Planetocosmics is valid for the scenario discussed here.

In sum, we use the same information on the shielding geometry as well as the same set of primary spectra for the cruise phase simulations as for the surface simulations. Cruise phase and surface simulations will be equally influenced by uncertainties produced by the primary spectra. However, the simulations reproducing the situation on the Martian surface only depend on the rover body shielding simulation as opposed all of the MSL cruise stage spacecraft needed for the cruise phase simulations. Thus, the uncertainties in shielding geometry and composition will have a lesser influence on surface simulations. Since we found good agreement between simulation and observation on the Martian surface, we conclude that the other sources of uncertainties discussed above do not play a major role.

6. Conclusions

We developed and demonstrated a method for distinguishing between upward and downward directed particle fluxes with the RAD instrument. After compiling known data for the geometry and composition of the shielding masses both during the cruise phase and on the Martian surface, we developed simulation models for both phases. For the cruise phase, reasonable agreement for the upward to downward ratio was found between RAD instrument data and simulation data. On the Martian surface, we found good agreement between simulation and observation data. While this will need to be confirmed e.g. by evaluating the upward and downward fluxes for particles other than protons, or by evaluating the fluxes for different time ranges on

the Martian surface, we conclude that we can simulate the Martian radiation environment in enough detail to reproduce our observations.

The method presented here allows for distinguishing between flux directions. It is also a first step in the goal of extending charged particle spectra measurements from the design limit of 10 MeV to 100 MeV stated in Hassler et al. (2012) up to 200 MeV. During the branch integration, the upward and downward fluxes in that energy range are integrated. The downward integrated flux can directly be used as an extension of the existing flux histograms. This will be a significant extension of the instruments' design capabilities as outlined in Hassler et al. (2012) and will be of considerable value for future work. The method is also an implementation of the idea to use particles penetrating the detector stack for in-depth analysis as outlined in Posner et al. (2005).

Acknowledgments

RAD is supported by NASA (HEOMD) Mars Science Laboratory Mission and Science Investigation, under JPL subcontract 1273039 to Southwest Research Institute and in Germany by DLR and DLR's Space Administration grants 50QM0501 and 50QM1201 to the Christian Albrechts University, Kiel. Part of this research was carried out at the Jet Propulsion Laboratory, California Institute of Technology, under a contract with the National Aeronautics and Space Administration. In particular, we would like to extend sincere gratitude to Jeff Simmonds, Ashwin Vasavada, and Joy Crisp at JPL, Gale Allen, Michael Meyer, Chris Moore, Victoria Friedensen at NASA HQ, and Heiner Witte at DLR in Germany for their unwavering support of RAD over the years. The RAD instrument data used in the analysis presented here are available in the NASA Planetary Data System at <http://ppi.pds.nasa.gov/search/view/?f=yes&id=pds://PPI/MSL-M-RAD-2-EDR-V1.0>

References

- Agostinelli, S., Allison, J., Amako, K., Apostolakis, J., Araujo, H., Arce, P., ... Zschesche, D. (2003). Geant4—A simulation toolkit. *Nuclear Instruments and Methods in Physics Research Section A: Accelerators, Spectrometers, Detectors and Associated Equipment*, 506(3), 250–303. [https://doi.org/10.1016/S0168-9002\(03\)01368-8](https://doi.org/10.1016/S0168-9002(03)01368-8)
- Allison, M. (1997). Accurate analytic representations of solar time and seasons on Mars with applications to the Pathfinder/Surveyor missions. *Geophysical Research Letters*, 24, 1967–1970. <https://doi.org/10.1029/97GL01950>
- Böhm, E. (2004). Neutron detection with scintillation counters (Tech. Rep.). Kiel, Germany: Christian-Albrechts-University of Kiel.
- Desorgher, L., Flückiger, E. O., & Gurtner, M. (2006). The PLANETOCOSMICS Geant4 application. In *36th COSPAR Scientific Assembly*. Beijing.
- Edquist, K. T., Hollis, B. R., Johnston, C. O., Bose, D., White, T. R., & Mahzari, M. (2014). Aerothermodynamic design of the Mars Science Laboratory heatshield. *Journal of Spacecraft and Rockets*, 51(4), 1106–1124. <https://doi.org/10.2514/6.2009-4078>
- Ehresmann, B., Zeitlin, C., Hassler, D. M., Wimmer-Schweingruber, R. F., Böhm, E., Böttcher, S., ... Reitz, G. (2014). Charged particle spectra obtained with the Mars Science Laboratory Radiation Assessment Detector (MSL/RAD) on the surface of Mars. *Journal of Geophysical Research: Planets*, 119, 468–479. <https://doi.org/10.1002/2013JE004547>
- Forget, F., Millour, E., & Lebonnois, S. (2006). The new Mars climate database. In *Second workshop on Mars atmosphere modelling and observations*. Granada, Spain.
- Gieseeler, J., & Heber, B. (2016). Spatial gradients of GCR protons in the inner heliosphere derived from Ulysses COSPIN/KET and PAMELA measurements. *Astronomy & Astrophysics*, 589, A32. <https://doi.org/10.1051/0004-6361/201527972>
- Gronoff, G., Norman, R. B., & Mertens, C. J. (2015). Computation of cosmic ray ionization and dose at Mars. I: A comparison of HZETRN and Planetocosmics for proton and alpha particles. *Advances in Space Research*, 55(7), 1799–1805. <https://doi.org/10.1016/j.asr.2015.01.028>
- Grotzinger, J. P., Crisp, J., Vasavada, A. R., Anderson, R. C., Baker, C. J., Barry, R., ... Wiens, R. C. (2012). Mars Science Laboratory Mission and science investigation. *Space Science Reviews*, 170, 5–56. <https://doi.org/10.1007/s11214-012-9892-2>
- Guo, J., Zeitlin, C., Wimmer-Schweingruber, R. F., Rafkin, S., Hassler, D. M., Posner, A., ... Reitz, G. (2015). Modeling the variations of dose rate measured by RAD during the first MSL Martian year: 2012–2014. *The Astrophysical Journal*, 810(1), 24. <https://doi.org/10.1088/0004-637X/810/1/24>
- Haberle, R. M., Gomez-Elvira, J., de la Torre Juarez, M., Harri, A.-M., Hollingsworth, J. L., Kahanpää, H., ... Zorzano-Mier, M.-P. (2014). Preliminary interpretation of the REMS pressure data from the first 100 sols of the MSL mission. *Journal of Geophysical Research: Planets*, 119, 440–453. <https://doi.org/10.1002/2014JE004657>. Received
- Hassler, D. M., Zeitlin, C., Wimmer-Schweingruber, R. F., Böttcher, S., Martin, C., Andrews, J., ... Cucinotta, F. A. (2012). The radiation assessment detector (RAD) investigation. *Space Science Reviews*, 170(1–4), 503–558. <https://doi.org/10.1007/s11214-012-9913-1>
- Hassler, D., Zeitlin, C., Wimmer-Schweingruber, R. F., Ehresmann, B., Rafkin, S., Eigenbrode, J. L., ... t. M. S. Team (2014). Mars' surface radiation environment measured with the Mars Science Laboratory's curiosity rover. *Science*, 343(6169), 1244,797–1244,797. <https://doi.org/10.1126/science.1244797>
- Matthiä, D., Ehresmann, B., Lohf, H., Köhler, J., Zeitlin, C., Appel, J., ... Wimmer-Schweingruber, R. F. (2016). The Martian surface radiation environment—A comparison of models and MSL/RAD measurements. *Journal of Space Weather and Space Climate*, 6, A13. <https://doi.org/10.1051/swsc/2016008>
- McDonald, F. B., & Ludwig, G. H. (1964). Measurement of low-energy primary cosmic-ray protons on IMP-1 satellite. *Physical Review Letters*, 13(26), 783–785. <https://doi.org/10.1103/PhysRevLett.13.783>
- Morthekai, P., Jain, M., Dartnell, L., Murray, A., Bøtter-Jensen, L., & Desorgher, L. (2007). Modelling of the dose-rate variations with depth in the Martian regolith using GEANT4. *Nuclear Instruments and Methods in Physics Research Section A: Accelerators, Spectrometers, Detectors and Associated Equipment*, 580(1), 667–670. <https://doi.org/10.1016/j.nima.2007.05.118>
- Müller-Mellin, R., Kunow, H., Fleißner, V., Pehlke, E., Rode, E., Röschmann, N., ... Henrion, J. (1995). COSTEP—Comprehensive suprathermal and energetic particle analyser. In B. Fleck, V. Domingo, & A. Poland (Eds.), *The SOHO mission* (pp. 483–504). Dordrecht: Springer Netherlands. https://doi.org/10.1007/978-94-009-0191-9_13
- Niita, K., Sato, T., Iwase, H., Nose, H., Nakashima, H., & Sihver, L. (2006). PHITS—a particle and heavy ion transport code system. *Radiation Measurements*, 41(9–10), 1080–1090. <https://doi.org/10.1016/j.radmeas.2006.07.013>
- Ogunniyi, I. O., Vermaak, M. K. G., & Groot, D. R. (2009). Chemical composition and liberation characterization of printed circuit board comminution fines for beneficiation investigations. *Waste management (New York, N.Y.)*, 29(7), 2140–6. <https://doi.org/10.1016/j.wasman.2009.03.004>
- O'Neill, P. (2010). Badhwar-o'Neill 2010 galactic cosmic ray flux model—Revised. *IEEE Transactions on Nuclear Science*, 57(6), 3148–3153. <https://doi.org/10.1109/tns.2010.2083688>
- Posner, A., Hassler, D. M., McComas, D. J., Rafkin, S., Wimmer-Schweingruber, R. F., Böhm, E., & Heber, B. (2005). A high energy telescope for the solar orbiter. *Advances in Space Research*, 36(8), 1426–1431. <https://doi.org/10.1016/j.asr.2004.11.040>
- Reitz, G., Berger, T., Bilski, P., Facius, R., Hajek, M., Petrov, V., ... Dettmann, J. (2009). Astronaut's organ doses inferred from measurements in a human phantom outside the international space station. *Radiation Research*, 171(2), 225–235. <https://doi.org/10.1667/RR1559.1>
- Sierks, H. (1997). Messung geladener teilchen mit dem kieler instrument EPHIN an bord der SOHO-raumsonde, Ph. D. thesis. Kiel, Germany: Christian-Albrechts-University of Kiel.
- Tran, H., Johnson, C., Rasky, D., Hui, F., Hsu, M.-T., & Chen, Y. (1996). Phenolic impregnated carbon ablators (PICA) for Discovery class missions. In *31st Thermophysics Conference*. Reston, Virginia: NASA, American Institute of Aeronautics and Astronautics. <https://doi.org/10.2514/6.1996-1911>

- Usoskin, I. G., Bazilevskaya, G. A., & Kovaltsov, G. A. (2011). Solar modulation parameter for cosmic rays since 1936 reconstructed from ground-based neutron monitors and ionization chambers. *Journal of Geophysical Research*, 116, A02104. <https://doi.org/10.1029/2010JA016105>
- Wimmer-Schweingruber, R. F., Köhler, J., Hassler, D. M., Guo, J., Appel, J.-K., Zeitlin, C., ... Cucinotta, F. (2015). On determining the zenith angle dependence of the Martian radiation environment at Gale Crater altitudes. *Geophysical Research Letters*, 42, 10,557–10,564. <https://doi.org/10.1002/2015GL066664>
- Zeitlin, C., Hassler, D. M., Cucinotta, F. A., Ehresmann, B., Wimmer-Schweingruber, R. F., Brinza, D. E., ... Reitz, G. (2013). Measurements of energetic particle radiation in transit to mars on the Mars Science Laboratory. *Science*, 340(6136), 1080–1084. <https://doi.org/10.1126/science.1235989>